Subwavelength confinement of propagating surface acoustic waves

B. J. Ash, A. R. Rezk, L. Y. Yeo, and G. R. Nash

View Online   Export Citation   CrossMark

ARTICLES YOU MAY BE INTERESTED IN

AIP Publishing

Subwavelength confinement of propagating surface acoustic waves

B. J. Ash,[1] A. R. Rezk,[2] L. Y. Yeo,[2] and G. R. Nash[1,a]

AFFILIATIONS

[1]College of Engineering, Mathematics and Physical Sciences, University of Exeter, Exeter EX4 4QF, United Kingdom
[2]Micro/Nanophysics Research Laboratory, School of Engineering, RMIT University, Melbourne, Victoria 3000, Australia

a)Author to whom correspondence should be addressed: g.r.nash@exeter.ac.uk

ABSTRACT

The ability to confine light to subwavelength scales has led to exciting developments in fields ranging from sensing to single molecule chemistry. In this paper, we demonstrate how arrays of annular hole resonators can be used to confine surface acoustic waves (SAWs) to regions of the propagating surface that are much smaller than the wavelength of the SAWs. These microscopic elastic waves are used in devices for signal processing and sensing and, increasingly, in areas such as quantum information and microfluidics. This work potentially transforms the ability to enhance interactions with SAWs and could pave the way for advances that mirror those in nano-photonics.

Published by AIP Publishing. https://doi.org/10.1063/5.0038381

Since 1855,[1] the investigation of the properties of surface acoustic waves (SAWs) has been a vibrant area of research and innovation. The invention of the interdigital transducer (IDT) in the 1960s,[2] which allows SAWs to be directly excited on the surface of a piezoelectric crystal, led to the rapid development of devices that underpin many sensing and signal processing systems. There has been considerable recent interest in the use of SAWs for quantum information, microfluidics, and integration with both 2D materials and optomechanical systems, see, for example, Refs. 3–11. However, up until this point, it has been impossible to confine the energy of a propagating SAW into a region on the propagation surface smaller than its wavelength. As with photonics,[12] the ability to effectively control and confine the SAWs in subwavelength structures would lead to new device concepts and paradigms, for example, the potential for increased sensitivity chemical or gas sensing using highly resonant cavities.

One of the most promising ways of controlling SAWs is through the use of phononic crystals (PnCs), which can be engineered to exhibit complete bandgaps (see, for example, Refs. 13–16) prohibiting propagation. Such structures are being investigated for the shaping of fluid droplets,[17] superlensing effects,[18–20] to provide an acoustic analogue to both graphene and topological materials,[21–23] and to create waveguides and cavities.[24,25] Gradient-index phononic crystals, such as those pioneered by Lin *et al.*,[26] have also been used to focus elastic waves.[27,28] Socié *et al.*[29] laterally confined SAWs between the electroplated fingers of an interdigital transducer, but the confinement was not subwavelength due to the reduced phase velocities of the confined modes.

Much early research in phononics focused on approaches that were direct analogs of designs used in photonics, and a commonly used design for SAW PnCs is that of etched holes in substrates where bandgaps are defined by the pitch and filling fraction of periodic arrays through Bragg scattering.[30,31] More recently, arrays consisting of local resonators have been shown to offer greater design freedom as bandgap frequencies and other characteristics are defined not only by the periodicity of the phononic crystal but also by the properties of the resonators themselves. This allows, for example, bandgap frequencies to be tuned below the soundline within the first Brillouin zone, leading to arrays consisting of finite depth holes being viable without radiative coupling to bulk acoustic waves in the substrate medium.[32,33] In arrays of pillars, coupling between the pillar resonances and SAWs contributes to the formation of a bandgap,[34,35] whereas locally resonant annular- and spiral-holes were also found to induce bandgaps but with extraordinary extinction ratios.[36,37]

Confinement of SAWs using resonating elements has been achieved experimentally through the graded system of a metawedge exhibiting rainbow trapping,[38] a concept that has recently been extended by combination with a topological insulator,[39] and in single resonators at the focus of quasiannular IDTs.[40] These works report stationary confinement with zero group velocities, but for many applications, it is desirable for propagating SAWs to be able to couple in and out of the confining region so that the intensity and phase of a single SAW can be measured as it interacts with an array of confining regions, defined in the propagating path as required. This design

principle has been acknowledged in the plasmon analogue, where propagating surface plasmon polaritons on metal films are more suitable for solid-state lighting applications than localized plasmons in nanoparticles because photo-emitters are coupled over a much larger area.[41] A numerical demonstration of PnC waveguides including subwavelength defect resonators has been achieved[42] but not realized experimentally.

In this work, we show, through both modeling and experiments, that it is possible to confine propagating, plane wave SAWs, generated using conventional interdigital transducers (IDTs), in subwavelength regions of the propagating surface using arrays of annular hole resonators.

Arrays of resonators were patterned onto commercially available 128° YX-lithium niobate (LiNbO3) SAW delay line devices, as shown schematically in Fig. 1(a). These had an acoustic path length of 5.4 mm and two identical, uniform double-electrode input/output transducers, designed to give resonances at a number of frequencies, and with a transducer aperture of 3.25 mm. Devices were mounted onto printed circuit boards using conductive silver epoxy, and measurements were undertaken at room temperature.

The system used in this work consists of a square array, with pitch A, of two different types of annular hole resonators, as illustrated in Fig. 1(b). The two types of resonators are identical, apart from their depth. In the remainder of the manuscript, resonators with smaller and larger depths are referred to as standard and defect resonators, respectively. Standard annular hole resonators have a finite depth D_S and radius R, whereas defect resonators have the same radius but larger depths, D_D ($D_D > D_S$). In the fabricated devices, a single line of defect resonators (each with the same depth) was incorporated into an array of standard resonators, as shown schematically in Fig. 1(c).

The central part of the line of defect resonators, consisting of three resonators and outlined in red, was separated from the other parts of the line (outlined in green) by a small number of standard annular hole resonators. Although this arrangement superficially resembles an inline cavity between two waveguides, the system was not specifically designed to function as such but rather to provide the means to explore the excitation of the defect resonators by propagating SAWs.

Figure 1(d) shows an SEM image of a completed device where focused ion beam milling was used to fabricate the sample using established techniques,[34,43] with the fabrication method used here being the same as previously reported.[36] The specific dimensions used were A = 13.5 μm, R = 5.0 μm, D_S = 3.2 μm, D_D = 5.6 μm, S = 4A, and W = 3A, which were found to give significant displacements in the defect resonators. Finally, a laser Doppler vibrometry (LDV) system was used to scan the sample, measuring out-of-plane displacements from the surface.

The finite element method package COMSOL Multiphysics 5.3a was used for the simulations presented in this work. To calculate the band diagrams of arrays of resonators, an eigenfrequency domain model developed from Addouche et al.[42] was used, where the geometry consisted of an array of resonators at the top of an extended substrate as depicted in Fig. 1(b). A five unit wide supercell with four standard and one defect resonator was used, to calculate solutions to construct band diagrams, which allowed for a substrate depth of 15 A to be computed with the available resources. This depth is sufficient for the solved eigenfrequencies to converge at the frequencies of interest near the soundline, f_1, for example. To better approximate geometries that are achievable with the focused ion beam (FIB) milling used to fabricate the resonators, the depth profile of the resonators was considered to be conical in the model.
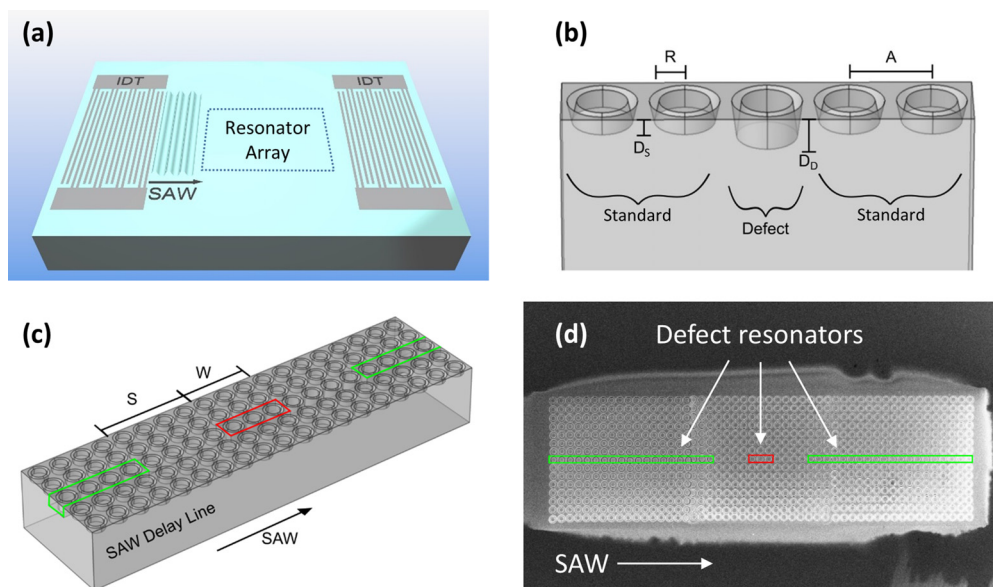

FIG. 1. (a) Device schematic showing the resonator array patterned between the interdigital transducers (IDTs) of a SAW delay line. (b) Schematic diagram of the resonator geometry, consisting of standard annular hole resonators of depth and radius of D_S and R, respectively, and defect resonators with the same radius but depth D_D. (c) Schematic diagram showing the separation of the three central defect resonators (red) from the line of other defect resonators (green). (d) SEM image of the fabricated array in LiNbO3, with the position of the defect resonators highlighted.

To investigate the size of the displacement excited in the resonators, a second model with an 11 resonator wide supercell, with 10 standard and one defect resonators, was used in order to investigate the behavior away from the central defects. The five unit wide supercell results were used to inform the 11 unit simulation parameters. In both cases, Bloch-Floquet periodic boundary conditions assume an infinitely large square array in the propagation direction, which is from left to right in Fig. 1(a) and into the image in Fig. 1(b). A fixed constraint boundary condition was applied to the bottom of the geometry to prevent plate modes from being solved.

As described above, an established method[35,43,44] was first used to calculate the dispersions of a system consisting of a single line of defect resonators incorporated into an array of standard resonators. Note that to enable the calculation of bandstructures, the line of defector resonators was continuous, without the central portion being isolated. The calculated eigenfrequencies are plotted against the wavevector within the first Brillouin zone in Fig. 2(a). The shaded gray region in the band diagram is above the soundline where SAW modes are radiative,[43,45] and solutions in this region were excluded. The highlighted frequencies f_1 and f_2 represent modes within the resonator array (at frequencies of 97 MHz and 108 MHz) that arise due to the inclusion of the line of defect resonators [note that these modes are not present in the dispersion in an array consisting of just standard annular hole resonators, as shown in Fig. 2(e)]. The frequency f_3 represents a control frequency used in the experimental results (33 MHz). The modes associated with the line of defect resonators are not independent of wavevector across the Brillouin zone, which we believe is due to the coupling of stationary modes associated with the defect resonators to propagating bands within the resonator array (i.e., bands at lower frequencies and close to the Rayleigh line[33]). This results in hybridized modes with a branch that has zero group velocity solutions at the Brillouin zone boundary and a branch that crosses the Rayleigh line. The solutions where the calculated coupled bands cross the solid black Rayleigh SAW line, at frequencies f_n, are labeled as M_n. These modes are, therefore, associated with the line of defect resonators but can be excited with a propagating SAW generated using an interdigital transducer.

This is confirmed by the calculated surface displacements at the frequencies associated with these modes, and the RMS (root mean square) surface displacement within the supercell for mode M_1 is shown in Fig. 2(b) (note that the RMS displacement shown here includes the in-plane components and is defined as $\frac{1}{\sqrt{2}}\sqrt{A_x^2 + A_y^2 + A_z^2}$, where A_x, A_y, and A_z are the amplitudes of the displacement field in the x, y, and z directions, respectively). The largest surface displacement is observed at the position of the defect resonator, with minimum RMS displacement within the two nearest standard resonators on either side of the defect resonator. The SAW is, therefore, being confined within a portion of the array that has a width that is subwavelength, as the diameter of one defect resonator ($10\,\mu m$) is smaller than the SAW wavelength ($40\,\mu m$). Interestingly, further away at the edges of the supercell, there are Rayleigh-like displacement profiles within the resonator array, which results from M_1 being a hybridized mode with similar group and phase velocities as the Rayleigh SAW.

To investigate the excitation of the defect resonators in the case where the line of defects is not continuous, as in Fig. 1(c), a separate
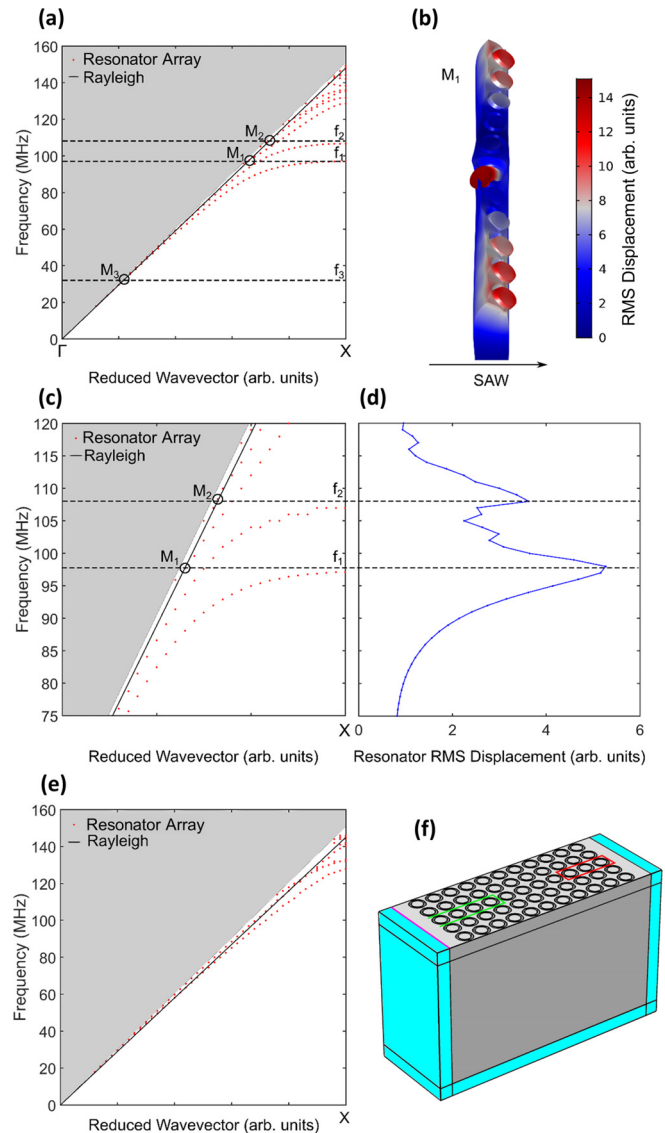

FIG. 2. (a) Band diagram, below the soundline and within the first Brillouin zone, of the resonator array obtained from the five resonator supercell. The red points are the calculated solutions within the array, the solid black line is the linear Rayleigh wave dispersion, the dashed black lines highlight the frequencies f_n and the modes M_n are where the Rayleigh line crosses the calculated bands at these frequencies. (b) RMS displacement surface plot in the 11 resonator supercell of mode M_1, (c) magnified section of the band diagram alongside, and (d) the average RMS displacement within the defect resonators that form the cavity, with a common frequency axis. (e) Band diagram, below the soundline and within the first Brillouin zone, of an array consisting of only standard annular hole resonators. The red points are the calculated array solutions, and the solid black line is the linear Rayleigh wave dispersion. (f) Finite sized array model used for frequency domain simulations, which was used to calculate the resonator RMS displacement as a function of the frequency (d). The cyan shaded domains represent perfectly matched layers used for absorption, the green and red outlined areas represent the waveguide and in-line cavity regions, respectively, and the pink line represents the SAW source.

frequency domain model of a finite-sized array representative of the fabricated device shown in Fig. 1 was used, comprising a 5 × 11 finite size square array geometry, as shown in Fig. 2(f), with defect resonators highlighted. Perfectly matched layers reduce acoustic reflections, an edge load source excites plane wave SAWs, and a frequency domain solver is used over swept frequencies.

In Fig. 2(d), the calculated average RMS displacement of the central, isolated, defect resonators is plotted as a function of frequency alongside a magnified section of the supercell band diagram. Two clear maxima are observed in the displacement, corresponding to the frequencies f_1 and f_2. In the simulation, a Rayleigh SAW source is used, meaning that these peaks arise from the excitation of modes M_1 and M_2 associated with the line of defect resonators, where the wavevectors are matched to the Rayleigh line.

The fabricated device was characterized using laser Doppler vibrometry to verify the results obtained through simulations. The spatial scan density was set to allow for at least 10 points per wavelength. Figure 3 shows the LDV measurements at the resonant SAW frequency of 97 MHz, where the black dashed rectangle in Fig. 3(a) indicates central defect resonators, as outlined in red in Fig. 1. A large displacement can be seen in the three central defect resonators in Figs. 3(a), 3(b), and 3(d), where the amplitude of the time averaged

displacement is plotted [Fig. 3(b) is a magnified view of the region around the central resonators]. The strong displacement observed within these resonators, as shown in the cross section plotted in Fig. 3(d), is consistent with the results of the simulations plotted in Fig. 2(c). The measurements yielded a value of ~140 pm displacement within the central defect resonator of the cavity, compared to a minimum of 30 pm outside it. The time averaged displacement shows stationary, non-propagating modes, in addition to propagating modes, whereas the instantaneous displacement, as plotted in Fig. 3(c), shows only propagating modes (note that the measured displacement is still time-averaged with regard to the vertical oscillations of the surface, which occur at 97 MHz, but is instantaneous with respect to the propagation of the wave, which propagates with a velocity of ~100 m/s, such that stationary modes are not visible). In this case, there is no observable displacement within the central resonators. This suggests that the resonators act to confine the propagating SAWs in two dimensions, parallel and perpendicular to the propagation direction, over scales much smaller than the wavelength.

Although fabrication errors are clearly seen in the patterning of the array [Fig. 1(d)], for example, stitching errors at the bottom of the device lead to the displacement of subsequent rows, the array still functions as intended. This is due to the periodicity of the array not
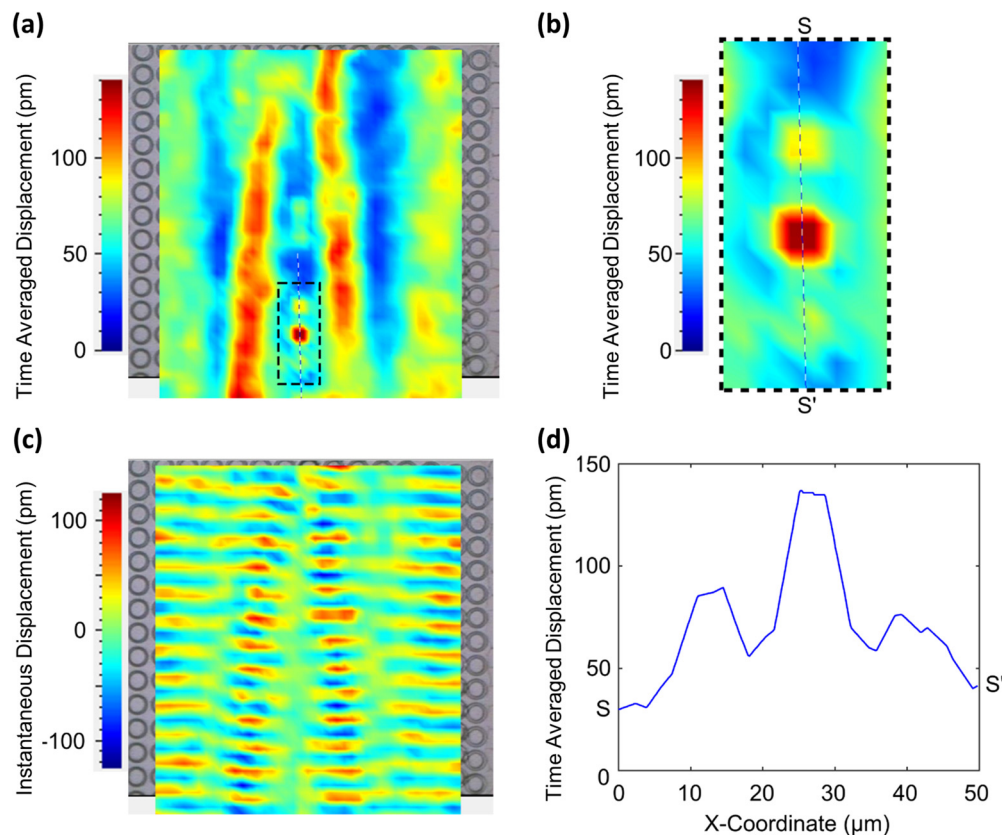

FIG. 3. Experimental results at the confinement frequency (a) amplitude of the time averaged displacement color plot overlaid on top of an image of the fabricated device, with the three central defect resonators outlined by a black dashed rectangle, at 97 MHz, (b) magnified section of the central region from the displacement plot in (a), (c) instantaneous displacement color plot of the same scan in (a), and (d) line plot of the time averaged displacement along the cross section line S–S′ in the center of three defect resonators in (b). Note that the SAW is propagating from bottom to top in the scans shown in (a), (b), and (c).

being the origin of the confinement, in contrast to conventional phononic crystals. This resilience to array aberrations has been reported previously where pseudo-random arrangements of locally resonant PnCs retain locally resonant bandgaps.[33]

The ability to excite displacements within these subwavelength structures is due to the matching of velocities between the hybridized modes, associated with the defect resonators, and propagating Rayleigh waves. At the resonant frequencies of the resonators, this results in the impedance mismatch being minimized and, therefore, a reduced reflection coefficient. For mode M_1, the absolute characteristic impedance is $Z = 1.2 \times 10^7$ Rayls, whereas for the Rayleigh SAW, $Z = 1.9 \times 10^7$ Rayls, leading to a reflection coefficient $\Gamma_R = 0.23$. The impedance Z was calculated from the density, ρ, and group velocity of the medium, ν ($Z = \rho\nu$). The reflection coefficient, Γ_R, at the interface between two media with characteristic impedances Z_1 and Z_2 is then given by $\Gamma_R = (Z_2 - Z_1)/(Z_2 + Z_1)$.

However, a low value of reflection coefficient is not always obtained for different geometries. Figure 4 shows simulated characterization of a modified supercell, but with much deeper hole depths of $D_S = 15 \, \mu m$ and $D_D = 26 \, \mu m$ (as compared to $D_S = 3.2 \, \mu m$ and $D_D = 5.6 \, \mu m$ previously). With an increased depth to pitch ratio associated with this change, the mode [Fig. 4(a)] associated with the defect resonators, M_4 (at a frequency of ~11 MHz), is deeply subwavelength, with the diameter of the defect resonator (10 μm) being approximately 40 times smaller than the SAW wavelength (~360 μm) at this frequency. While there is significant displacement within the defect resonators, as shown in Fig. 4(b), the group velocity of this mode, 74 m/s, is over an order of magnitude slower than the Rayleigh SAW. This leads to a characteristic impedance of $Z = 3.5 \times 10^5$ Rayls and a reflection coefficient of $\Gamma_R = 0.96$, so these slow modes could not be excited by a propagating SAW, without applying other coupling techniques. For example, it may be possible to do this using a graded structure, in analogy to a graded dielectric index material, where the depth of the holes of the resonators is slowly increased over distance. A second higher frequency mode, M_5, has a group velocity similar to the

Rayleigh line and could, therefore, be excited by a propagating SAW, but in this case, the resultant displacement, Fig. 4(c), is not confined to the defect resonators.

Finally, the ability to define subwavelength regions in which a propagating SAW can be confined, using a local resonator approach, offers a potential avenue to increase the sensitivity and functionality of SAW sensors. Small changes to the environment of a resonating element, for example, changes to gas pressure, are likely to have a significant effect on the characteristics of the SAW propagating beyond the confining region, which would give rise to the sensing signal. Subwavelength confinement could also allow the use of SAWs to probe entities that are much smaller than the SAW wavelength although it should be noted that the geometries presented in this work have not yet been optimized and further work is therefore under way to establish design rules for the realization of arrays optimized for different applications.

In conclusion, finite element simulations show that the incorporation of a line of defect resonators within an array of annular hole resonators creates new modes in the dispersion diagram. These modes appear to be hybridized modes that cross the Rayleigh dispersion at the resonant frequencies and which have similar group velocities to the propagating SAW at these wavevectors such that they can be excited using plane wave SAWs generated from standard transducers. A separate frequency domain model of a finite-sized array, consisting of three, isolated defect references in the center of the line, was used to show that it is possible to confine the SAW, both parallel and perpendicular to the propagation direction, over length scales much smaller than the SAW wavelength.

An array fabricated in a LiNbO$_3$ delay line was characterized via laser Doppler vibrometry to verify the simulations. Strong displacements were observed in the defect resonators, at the resonant frequency of 97 MHz, confirming the confinement seen in the simulations. These results pave the way for devices exploiting subwavelength SAW confinement, allowing developments in phononics to mirror those that have occurred in photonics.
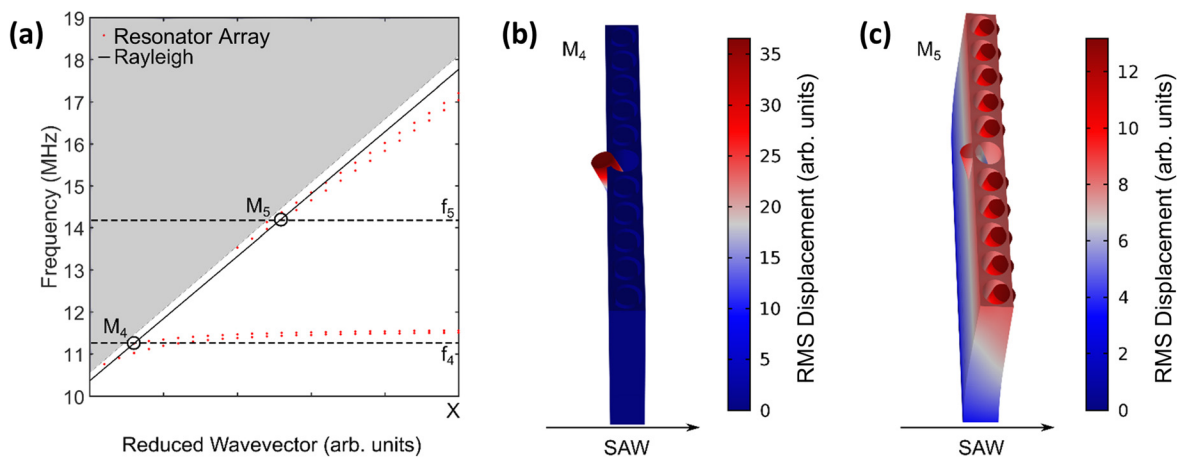

FIG. 4. Characterization of a "deep" subwavelength line of defect resonators. (a) Band diagram of a resonator array, incorporating a deep subwavelength line of defects, composed of both standard and defect annular holes of much greater depth. The red points are the calculated solutions within the array, the solid black line is the linear Rayleigh wave dispersion, the dashed black lines highlight the frequencies f_n and the modes M_n are where the Rayleigh line crosses the calculated bands at these frequencies. (b) and (c) RMS displacement surface plot in the supercell of modes M_4 and M_5, respectively.

DATA AVAILABILITY

The data that support the findings of this study are available from the corresponding author upon reasonable request.

REFERENCES

[1] L. Rayleigh, Proc. London Math. Soc. **s1–17**, 4 (1885).

[2] R. M. White and F. W. Voltmer, Appl. Phys. Lett. **7**, 314 (1965).

[3] S. Hermelin, S. Takada, M. Yamamoto, S. Tarucha, A. D. Wieck, L. Saminadayar, C. Bauerle, and T. Meunier, Nature **477**, 435 (2011).

[4] R. P. G. McNeil, M. Kataoka, C. J. B. Ford, C. H. W. Barnes, D. Anderson, G. A. C. Jones, I. Farrer, and D. A. Ritchie, Nature **477**, 439 (2011).

[5] L. Y. Yeo and J. R. Friend, Annu. Rev. Fluid Mech. **46**, 379 (2014).

[6] D. J. Collins, B. Morahan, J. Garcia-Bustos, C. Doerig, M. Plebanski, and A. Neild, Nat. Commun. **6**, 8686 (2015).

[7] G. Destgeer and H. J. Sung, Lab Chip **15**, 2722 (2015).

[8] D. B. Go, M. Z. Atashbar, Z. Ramshani, and H.-C. Chang, Anal. Methods **9**, 4112 (2017).

[9] E. Preciado, F. J. R. Schülein, A. E. Nguyen, M. Barroso, M. Isarraraz, G. von Son, I.-H. Lu, W. Michailow, B. Möller, V. Klee, J. Mann, A. Wixforth, and L. Bartels, Nat. Commun. **6**, 8593 (2015).

[10] K. C. Balram, M. I. Davanço, J. D. Song, and K. Srinivasan, Nat. Photonics **10**, 346 (2016).

[11] P. Delsing, A. N. Cleland, M. J. A. Schuetz, J. Knörzer, G. Giedke, J. I. Cirac, K. Srinivasan, M. Wu, K. C. Balram, C. Bäuerle, T. Meunier, C. J. B. Ford, P. V. Santos, E. Cerda-Méndez, H. Wang, H. J. Krenner, E. D. S. Nysten, M. Weiß, G. R. Nash, L. Thevenard, C. Gourdon, P. Rovillain, M. Marangolo, J.-Y. Duquesne, G. Fischerauer, W. Ruile, A. Reiner, B. Paschke, D. Denysenko, D. Volkmer, A. Wixforth, H. Bruus, M. Wiklund, J. Reboud, J. M. Cooper, Y. Fu, M. S. Brugger, F. Rehfeldt, and C. Westerhausen, J. Phys. D: Appl. Phys. **52**, 353001 (2019).

[12] A. F. Koenderink, A. Alù, and A. Polman, Science **348**, 516 (2015).

[13] W. Cheng, J. Wang, U. Jonas, G. Fytas, and N. Stefanou, Nat. Mater. **5**, 830 (2006).

[14] Y. F. Wang, Y. S. Wang, and X. X. Su, J. Appl. Phys. **110**, 113520 (2011).

[15] R. Pourabolghasem, S. Mohammadi, A. A. Eftekhar, A. Khelif, and A. Adibi, Appl. Phys. Lett. **105**, 231908 (2014).

[16] J. A. Kulpe, K. G. Sabra, and M. J. Leamy, J. Acoust. Soc. Am. **139**, 3009 (2016).

[17] Y. Bourquin, R. Wilson, Y. Zhang, J. Reboud, and J. M. Cooper, Adv. Mater. **23**, 1458 (2011).

[18] M. Addouche, M. A. Al-Lethawe, A. Choujaa, and A. Khelif, Appl. Phys. Lett. **105**, 023501 (2014).

[19] X. Zhang and Z. Liu, Appl. Phys. Lett. **85**, 341 (2004).

[20] M.-H. Lu, C. Zhang, L. Feng, J. Zhao, Y.-F. Chen, Y.-W. Mao, J. Zi, Y.-Y. Zhu, S.-N. Zhu, and N.-B. Ming, Nat. Mater **6**, 744 (2007).

[21] D. Torrent and J. Sánchez-Dehesa, Phys. Rev. Lett. **108**, 174301 (2012).

[22] S.-Y. Yu, X.-C. Sun, X. Ni, Q. Wang, X.-J. Yan, C. He, X.-P. Liu, L. Feng, M.-H. Lu, and Y.-F. Chen, Nat. Mater. **15**, 1243 (2016).

[23] H. He, C. Qiu, L. Ye, X. Cai, X. Fan, M. Ke, F. Zhang, and Z. Liu, Nature **560**, 61 (2018).

[24] S. Benchabane, O. Gaiffe, R. Salut, G. Ulliac, V. Laude, and K. Kokkonen, Appl. Phys. Lett. **106**, 081903 (2015).

[25] D. Hatanaka and H. Yamaguchi, Phys. Rev. Appl. **13**, 024005 (2020).

[26] S.-C. S. Lin and T. J. Huang, Phys. Rev. B **79**, 094302 (2009).

[27] T.-T. Wu, Y.-T. Chen, J.-H. Sun, S.-C. S. Lin, and T. J. Huang, Appl. Phys. Lett. **98**, 171911 (2011).

[28] J. Zhao, R. Marchal, B. Bonello, and O. Boyko, Appl. Phys. Lett. **101**, 261905 (2012).

[29] L. Socié, S. Benchabane, L. Robert, A. Khelif, and V. Laude, Appl. Phys. Lett. **102**, 113508 (2013).

[30] S. Benchabane, O. Gaiffe, G. Ulliac, R. Salut, Y. Achaoui, and V. Laude, Appl. Phys. Lett. **98**, 171908 (2011).

[31] R. Zhu, X. N. Liu, G. K. Hu, C. T. Sun, and G. L. Huang, Nat. Commun. **5**, 5510 (2014).

[32] Y. Pennec, B. Djafari-Rouhani, H. Larabi, J. O. Vasseur, and A. C. Hladky-Hennion, Phys. Rev. B **78**, 104105 (2008).

[33] T.-T. Wu, Z.-G. Huang, T.-C. Tsai, and T.-C. Wu, Appl. Phys. Lett. **93**, 111902 (2008).

[34] A. Khelif, Y. Achaoui, S. Benchabane, V. Laude, and B. Aoubiza, Phys. Rev. B **81**, 21403 (2010).

[35] Y. Achaoui, V. Laude, S. Benchabane, and A. Khelif, J. Appl. Phys. **114**, 104503 (2013).

[36] B. J. Ash, S. R. Worsfold, P. Vukusic, and G. R. Nash, Nat. Commun. **8**, 174 (2017).

[37] V. Kyrimi, B. J. Ash, and G. R. Nash, J. Phys. D: Appl. Phys. **52**, 345306 (2019).

[38] A. Colombi, D. Colquitt, P. Roux, S. Guenneau, and R. V. Craster, Sci. Rep. **6**, 27717 (2016).

[39] G. J. Chaplain, J. M. De Ponti, G. Aguzzi, A. Colombi, and R. V. Craster, Phys. Rev. Appl. **14**, 054035 (2020).

[40] S. Benchabane, R. Salut, O. Gaiffe, V. Soumann, M. Addouche, V. Laude, and A. Khelif, Phys. Rev. Appl. **8**, 034016 (2017).

[41] J. A. Schuller, E. S. Barnard, W. Cai, Y. C. Jun, J. S. White, and M. L. Brongersma, Nat. Mater. **9**, 193 (2010).

[42] M. Addouche, M. Al-Lethawe, A. Elayouch, and A. Khelif, AIP Adv. **4**, 124303 (2014).

[43] G. Si, A. J. Danner, S. L. Teo, E. J. Teo, J. Teng, and A. A. Bettiol, J. Vac. Sci. Technol., B **29**, 021205 (2011).

[44] M. Al Lethawe, M. Addouche, S. Benchabane, V. Laude, and A. Khelif, AIP Adv. **6**, 121708 (2016).

[45] S. Benchabane, A. Khelif, J.-Y. RauchRobert, and V. Laude, Phys. Rev. E **73**, 065601 (2006).